Eulerian/Lagrangian formulation for the elasto-capillary deformation of a flexible fibre

Lecrivain, G.; Grein, T. B. P.; Yamamoto, R.; Hampel, U.; Taniguchi, T.;

Originally published:

February 2020

Journal of Computational Physics 409(2020), 109324

DOI: https://doi.org/10.1016/j.jcp.2020.109324

Eulerian/Lagrangian formulation for the elasto-capillary deformation of a flexible fibre

Gregory Lecrivain[a,b,*], Taisa Beatriz Pacheco Grein[a,c], Ryoichi Yamamoto[1], Uwe Hampel[a,d], Takashi Taniguchi[1,*]

[a] *Helmholtz-Zentrum Dresden-Rossendorf, Institut für Fluiddynamik, Bautzner Landstraße 400, 01328 Dresden, Germany*
[b] *Kyoto University, Department of Chemical Engineering, Kyoto 615-8510, Japan*
[c] *Universidade Federal de Santa Catarina, Centro Tecnológico, Departamento de Engenharia Mecânica, 88040-970 Florianópolis, Brazil*
[d] *Technische Universität Dresden, Professur für Bildgebende Messverfahren für die Energie- und Verfahrenstechnik, 01062 Dresden, Germany*

Abstract

The capillary-induced bending of flexible fibres, a process also known as elasto-capillary deformation, is central to a variety of industrial and non-industrial applications, among which stand out textile flotation, stabilization of emulsions, micro-folding of elastic structures, and clogging of feather fibres by oil droplets. A consistent formulation for the direct numerical simulation of a flexible fibre interacting with a fluidic interface is presently suggested. The fibre is geometrically decomposed into a chain of spherical beads, which undergo stretching-bending-twisting interactions. The capillary force, acting at the three-phase contact line, is calculated using a ternary diffuse-interface model. In a first stage, the fibre deformation model and the ternary diffuse-interface model are validated against theoretical solutions. In a second stage, the two- and three-dimensional elasto-capillary bending of a fibre by an immersed droplet are numerically investigated. Partial wrapping and complete encapsulation could be simulated. The results show that the fibre curvature increases linearly with the square of the elasto-capillary length, for both low and large structural deformation.

Keywords: Elasto-capillary deformation, fibre at fluidic interface, ternary diffuse interface model, direct numerical simulation, droplet encapsulation.

1. Introduction

1.1. Elasto-capillary fibre deformation

At sub-millimetric scales, a fluid droplet can easily deform an elastic structure such as a fibre or an extremely thin planar sheet. The dominant capillary forces can even cause a complete encapsulation of the fluid droplet by the elastic structure. This mechanism, known as the elasto-capillary deformation of a microstructure, is central to a wide variety of industrial applications, among which stand out the separation of textile and paper fibres [1, 2], the micro-folding of elastic structures [3, 4], along with the stabilisation of emulsions by cellulose fibres [5, 6]. Notable non-industrial applications include, for instance, the clogging of feather fibres by oil droplets after an accidental ocean spills [7] and the coiling of filamentous molecules around droplet-like proteins [8]. Figure 1 shows a schematic diagram of the ternary system presently investigated. A fibre is initially brought in contact with an immersed droplet and eventually bends as a results of the capillary action. After equilibrium is reached, the internal beam forces cancel out the external capillary forces.

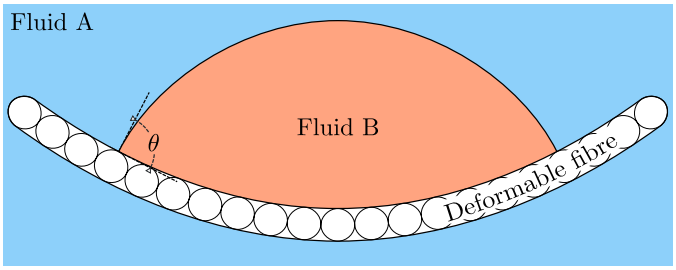

Figure 1: Schematic of the ternary system presently investigated. A fluid droplet deforms a fibre decomposed into a chain of N_b spherical beads.

1.2. Analytical elasto-capillary models

A number of analytical models have been suggested to simulate the elasto-capillary bending of fibres by fluid droplets. Most of the models recently reported in the literature were derived using a variational approach [9, 10], where the concept of force is not invoked. In the variational approach, the total energy of the system, composed of an interfacial energy and a bending structural energy, is minimised. Using a Lagrange multiplier to minimise the total energy, analytical solutions for the beam deformation could be suggested. Schulman et al. [11] used another approach based on the Bernoulli-Euler small beam theory to qualitatively compare the fibre curvature with experi-

*Corresponding authors
Email addresses: g.lecrivain@hzdr.de (Gregory Lecrivain), taniguch@cheme.kyoto-u.ac.jp (Takashi Taniguchi)

mental data. In the two-dimensional small beam theory, a homogeneously distributed load is assumed to cancel out the two meniscus forces acting on the fibre. The fibre profile is then solved by making the second space derivative $y''(x)$ proportional to the internal moment at the location x [12, 13].

1.3. Direct numerical simulation of deformable fibre in fluids

Most of the numerical advancement aimed at studying the dynamics of fibres immersed in a fluid was done for unary flow systems [14]. The idea behind decomposing the flexible fibre into a chain of bonded spheres and let it evolve dynamically with the fluid probably started with the pioneering work of Yamamoto and Matsuoka [15]. Various simulations, which also used a similar fibre decomposition into beads, later followed [16–20]. These previous studies essentially compared the dynamics of deformable fibres in laminar shear flows with those of rigid fibres. The tumbling period of a fairly rigid fibre in a shear flow was found to closely match the Jeffery's predictions for elongated prolates [19]. With increasing fibre flexibility, buckling and snaking fibre dynamics eventually occurred [21]. Recent activities by Dotto and Marchioli [22] seem to suggest an emerging research trend towards the study of fibre dynamics in turbulent shear flows.

1.4. Motivations

The above-mentioned studies inspired us to develop an alternative approach for the direct numerical simulation of deformable fibres in a binary fluid. Yet, we here focus on the unsteady elasto-capillary bending of a flexible fibre initially placed at a fluidic interface. Using a Lagrangian beam model [23, 24], the fibre is geometrically decomposed into a chain of spherical beads, which undergo stretching-bending-twisting structural interactions. The capillary force, acting at the three-phase contact line, is calculated using an Eulerian diffuse-interface model, which essentially tracks the deformation of the fluid/fluid and the fluid/solid interfaces [25]. To damp the unsteady dynamics of this ternary system, the viscous drag acting on each spherical bead is calculated using an Eulerian flow solver [26].

2. Methods

2.1. Lagrangian representation of the fibre

Let us first define an inertial frame $\boldsymbol{O}\boldsymbol{e}_x\boldsymbol{e}_y\boldsymbol{e}_z$, where $\boldsymbol{O}$ is a fixed origin and $\boldsymbol{e}_x$, $\boldsymbol{e}_y$, and $\boldsymbol{e}_z$ are the three unit vectors forming the Cartesian coordinate system. The fibre, which evolves in time and space, is decomposed into a chain of N_b spherical beads. The centre of mass of a single bead is located at the position $\boldsymbol{X}(t)$, where t is the time. The bead angular position is represented by a 4×1 row-matrix unit quaternion as

$$\boldsymbol{q}(t) = \begin{bmatrix} q_s \\ \boldsymbol{q}_v \end{bmatrix} = \begin{bmatrix} q_s \\ q_x \\ q_y \\ q_z \end{bmatrix} \tag{1}$$

where q_s is the scalar part and $\boldsymbol{q}_v = [q_x\, q_y\, q_z]^\top$ the vector part. A detailed introduction to rigid body dynamics in terms of quaternions may for instance be found in the book written by Huang [27] and in the paper written by Zhao and van Wachem [28]. The trajectory of each bead is solved independently as [29]

$$\frac{\mathrm{d}\boldsymbol{X}}{\mathrm{d}t} = \boldsymbol{V}, \tag{2}$$

$$\frac{\mathrm{d}\boldsymbol{q}}{\mathrm{d}t} = \frac{1}{2}\boldsymbol{A}\cdot\boldsymbol{q}, \tag{3}$$

where $\boldsymbol{V}$ is the bead translational velocity and $\boldsymbol{A}$ is a 4×4 orthogonal matrix given by

$$\boldsymbol{A} = \begin{bmatrix} 0 & -\Omega_x & -\Omega_y & -\Omega_z \\ \Omega_x & 0 & -\Omega_z & \Omega_y \\ \Omega_y & \Omega_z & 0 & -\Omega_x \\ \Omega_z & -\Omega_y & \Omega_x & 0 \end{bmatrix}. \tag{4}$$

The operator "$\cdot$" in Equation 3 denotes the product $A_{ij}q_j$ in the conventional ij-matrix notation. The rotational bead velocity is expressed in the inertial frame as $\boldsymbol{\Omega} = [\Omega_x\, \Omega_y\, \Omega_z]^\top$. The bead velocities are advanced in time as

$$m\frac{\mathrm{d}\boldsymbol{V}}{\mathrm{d}t} = \boldsymbol{F}^b + \boldsymbol{F}^h + \boldsymbol{F}^c + \boldsymbol{F}^e, \tag{5}$$

$$\boldsymbol{I}\cdot\frac{\mathrm{d}\boldsymbol{\Omega}}{\mathrm{d}t} = \boldsymbol{T}^b + \boldsymbol{T}^h + \boldsymbol{T}^c + \boldsymbol{T}^e, \tag{6}$$

where m is the mass of a single bead and $\boldsymbol{I}$ its moment of inertia. Note that, all beads have identical mass and moments of inertia. Because Equation 6 is solved in the body frame, the transformed moments of inertia actually form a constant diagonal tensor $\tilde{\boldsymbol{I}}$. The torques are also expressed in the body frame using the transformation $\tilde{\boldsymbol{T}} = \boldsymbol{R}^\top\cdot\boldsymbol{T}$, where $\boldsymbol{R}$ is the 3×3 rotation matrix associated with the bead quaternion $\boldsymbol{q}$. Details on how Equation 6 is solved can be found in the authors' previous work [30]. The term $\boldsymbol{F}^b$ is a "beam" force holding the beads of the fibre together, $\boldsymbol{F}^h$ a "hydrodynamic" drag force, $\boldsymbol{F}^c$ a "capillary" force responsible for the capillary-induced fibre deformation, and $\boldsymbol{F}^e$ an "external" force. In a similar fashion $\boldsymbol{T}^b$, $\boldsymbol{T}^h$, $\boldsymbol{T}^c$, and $\boldsymbol{T}^e$ are respectively the beam torque, the hydrodynamic torque, the capillary torque, and an external torque. The gravity and the hydrostatic contributions are here neglected because in most applications the capillary forces arising from the surface tension normally prevail by several orders of magnitude.

2.2. Calculation of the beam forces and beam torques

For the sake of simplicity, only the i-th bead and the j-th next neighbouring bead of a single fibre, with $j =$

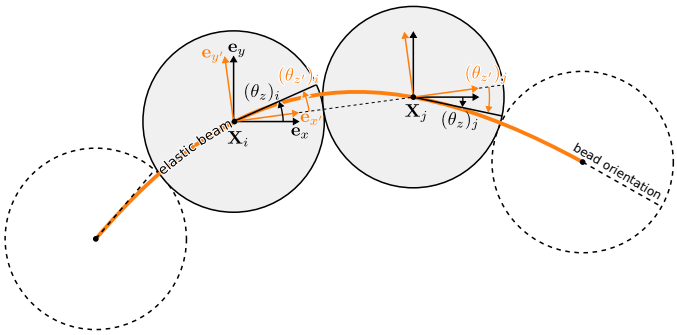

Figure 2: Two-dimensional visualisation of the virtual elastic beam connecting two successive beads of a fibre. The beam force reactions are conveniently expressed in the local beam frame $\boldsymbol{X}_i\boldsymbol{e}_{x'}\boldsymbol{e}_{y'}\boldsymbol{e}_{z'}$ shown in orange.

$i+1$, are considered in the present subsection. As illustrated in Figure 2, the two neighbouring beads are assumed to be connected by a virtual elastic beam. A number of beam models have been developed in the past to derive the beam forces acting on a discretised fibre portion [15, 18, 19, 24, 31–37]. A brief description of these available beam models can be found in the review provided by Guo and Curtis [38]. The so-called "cohesive beam model", originally suggested by Andre et al. [39] and derived analytically from the Euler-Bernoulli beam theory [12, 13], was here implemented. In this model, the beam forces and torques are expressed in a local beam frame $\boldsymbol{X}_i\boldsymbol{e}_{x'}\boldsymbol{e}_{y'}\boldsymbol{e}_{z'}$, where $\boldsymbol{e}_{x'}$ is the unit beam vector defined by

$$\boldsymbol{e}_{x'} = \frac{\boldsymbol{X}_j - \boldsymbol{X}_i}{|\boldsymbol{X}_j - \boldsymbol{X}_i|}. \tag{7}$$

The additional two unit vectors forming the local beam frame are given by

$$\boldsymbol{e}_{y'} = \boldsymbol{R}^* \cdot \boldsymbol{e}_y, \tag{8}$$
$$\boldsymbol{e}_{z'} = \boldsymbol{R}^* \cdot \boldsymbol{e}_z, \tag{9}$$

where $\boldsymbol{R}^*$ is the 3×3 rotation matrix resulting from the abscissa transformation $\boldsymbol{e}_x \to \boldsymbol{e}_{x'}$. The mathematical formulations of this rotation matrix and of its corresponding unit quaternion $\boldsymbol{q}^* = [q_s^*\, q_x^*\, q_y^*\, q_z^*]^\top$ are further detailed in Appendix A. The total beam force is then conveniently recast as

$$\boldsymbol{F}^b = F^b_{x'}\boldsymbol{e}_{x'} + F^b_{y'}\boldsymbol{e}_{y'} + F^b_{z'}\boldsymbol{e}_{z'}, \tag{10}$$

where $F^b_{x'}\boldsymbol{e}_{x'}$ is the structural force acting in the axial beam direction, and $F^b_{y'}\boldsymbol{e}_{y'} + F^b_{z'}\boldsymbol{e}_{z'}$ the structural force acting in the direction normal to the beam axis. The axial beam force components acting on the i-th and on the j-th bead are expressed as

$$\left(F^b_{x'}\right)_i = +\frac{\pi E r_b}{2}\Big(|\boldsymbol{X}_j - \boldsymbol{X}_i| - 2r_b\Big), \tag{11}$$
$$\left(F^b_{x'}\right)_j = -\left(F^b_{x'}\right)_i, \tag{12}$$

where E is the Young modulus with respect to fibre material and r_b the bead radius. Assuming a small deformation of the virtual elastic beam, the orientation angles of the i-th bead are approximated in the local beam frame as $(\theta_{x'})_i \approx 2(q_{x'})_i$, $(\theta_{y'})_i \approx 2(q_{y'})_i$, and $(\theta_{z'})_i \approx 2(q_{z'})_i$, where the vector part $[q_{x'}\, q_{y'}\, q_{z'}]^\top_i$ of the quaternion $\boldsymbol{q}'_i$ is derived from the following Hamilton product

$$\boldsymbol{q}'_i = \begin{bmatrix} q_{s'} \\ q_{x'} \\ q_{y'} \\ q_{z'} \end{bmatrix}_i = \boldsymbol{q}_i(\boldsymbol{q}^*)^{-1}. \tag{13}$$

The inverse unit quaternion, corresponding to the inverse frame transformation, is given by $(\boldsymbol{q}^*)^{-1} = [q_s^*\,, -q_x^*\,, -q_y^*\,, -q_z^*]^\top$. The approximation of the orientation angles at the j-th position is similarly derived from the Hamilton product $\boldsymbol{q}'_j = \boldsymbol{q}_j(\boldsymbol{q}^*)^{-1}$. Having defined the orientation angles in the local bead frame, the two beam force components acting in the first direction $\boldsymbol{e}_{y'}$ normal to the beam axis are given by

$$\left(F^b_{y'}\right)_i = -\frac{3\pi E r_b^2}{8}\Big[(\theta_{z'})_i + (\theta_{z'})_j\Big], \tag{14}$$
$$\left(F^b_{y'}\right)_j = -\left(F^b_{y'}\right)_i. \tag{15}$$

The beam force components acting in the second normal beam direction $\boldsymbol{e}_{z'}$ are given by

$$\left(F^b_{z'}\right)_i = +\frac{3\pi E r_b^2}{8}\Big[(\theta_{y'})_i + (\theta_{y'})_j\Big], \tag{16}$$
$$\left(F^b_{z'}\right)_j = -\left(F^b_{z'}\right)_i. \tag{17}$$

In a similar fashion, the beam torque is also decomposed in the local beam frame as

$$\boldsymbol{T}^b = T^b_{x'}\boldsymbol{e}_{x'} + T^b_{y'}\boldsymbol{e}_{y'} + T^b_{z'}\boldsymbol{e}_{z'}. \tag{18}$$

The i-th and j-th torsion-related torques acting in the axial beam direction are given by

$$\left(T^b_{x'}\right)_i = -\frac{\pi G r_b}{2}\Big[(\theta_{x'})_j - (\theta_{x'})_i\Big]\boldsymbol{e}_{x'}, \tag{19}$$
$$\left(T^b_{x'}\right)_j = -\left(T^b_{x'}\right)_i, \tag{20}$$

where G is the shear modulus with respect to the fibre material. The two components of the bending torque acting in the first direction $\boldsymbol{e}_{y'}$ normal to the beam axis are given by

$$\left(T^b_{y'}\right)_i = -\frac{\pi E r_b^3}{4}\Big[2(\theta_{y'})_i + (\theta_{y'})_j\Big], \tag{21}$$
$$\left(T^b_{y'}\right)_j = -\frac{\pi E r_b^3}{4}\Big[(\theta_{y'})_i + 2(\theta_{y'})_j\Big]. \tag{22}$$

Similarly, the two bending torque components in the second normal beam direction $\boldsymbol{e}_{z'}$ are given by

$$\left(T^b_{z'}\right)_i = -\frac{\pi E r_b^3}{4}\Big[2(\theta_{z'})_i + (\theta_{z'})_j\Big], \tag{23}$$
$$\left(T^b_{z'}\right)_j = -\frac{\pi E r_b^3}{4}\Big[(\theta_{z'})_i + 2(\theta_{z'})_j\Big]. \tag{24}$$

Owing to the use of quaternions, trigonometric functions are never used. This is a significant advantage of the present method.

2.3. Eulerian representation of the fibre

The fibre volume fraction $\phi(\boldsymbol{x},t)$ is introduced to represent the fibre in an Eulerian manner. This volume fraction will later be necessary to perform a volume integral and resolve the capillary and hydrodynamic forces. The sharp boundary of the i-th bead is here replaced with a smooth profile function $\phi_i(\boldsymbol{x},t)$, which undergoes a smooth but rapid transition from unity to zero as one moves from the inner bead region to the outer bead region [40]. A number of smooth profile functions are presented in the work of Nakayama and Yamamoto [41]. A truncated hyperbolic tangent profile is here chosen to mathematically represent the volume of each spherical bead. The smooth profile function of the i-th spherical bead takes the form

$$\phi_i(\boldsymbol{x},t) = \begin{cases} 1 & \text{if } |\boldsymbol{x}-\boldsymbol{X}_i| < r_b - \xi_c, \\ 0 & \text{if } |\boldsymbol{x}-\boldsymbol{X}_i| > r_b + \xi_c, \\ \frac{1}{2} + \frac{1}{2}\tanh\left(\frac{r_b - |\boldsymbol{x}-\boldsymbol{X}_i|}{\sqrt{2}\xi}\right) & \text{elsewhere,} \end{cases} \tag{25}$$

where ξ is the interfacial length and ξ_c is an arbitrarily set cut-off length. First, the cut-off length ξ_c is introduced to efficiently calculate the right hand sides of the later Equations 35 and 36, where the integrals $\int_{\mathcal{V}} \mathrm{d}\mathbf{x}$ run over the entire space of the domain. The truncation hence eliminates the far-off integration space for $|r_b - |\boldsymbol{x}-\boldsymbol{X}_i|| > \xi_c$, where $\phi_i(x) \approx 0$ [41]. The code implementation is also not yet fully optimized and has a rather weak scaling efficiency on high performance computers. Calling the hyperbolic tangent over the whole domain simply is more time consuming. Second, the value of the cut-off length, specified in the presented tests, has a negligible effect on the results because only a very small portion of the interfacial energy is stored in the truncated far-off tail. The profile summation ϕ, hereafter referred to as the fibre volume fraction, is defined by the superposition of the individual N_b smooth profile functions as

$$\phi(\boldsymbol{x},t) = \sum_{i=0}^{N_b-1} \phi_i(\boldsymbol{x},t). \tag{26}$$

2.4. Eulerian representation of the binary fluid

The fibre is immersed in a binary fluid, composed of a fluid constituent A and a fluid constituent B. The two volume fractions $\phi_A(\boldsymbol{x},t)$ and $\phi_B(\boldsymbol{x},t)$ are also introduced to represent each fluid constituent in an Eulerian manner. A variety of three-phase models have emerged in the recent years to study the dynamics of individual spherical beads in binary fluids [42–45]. A diffuse-interface approach [46] is here employed to simulate the separation of the binary fluid into its two fluid immiscible constituents A and B. The dynamics of the separation is driven by the minimisation of a free energy $\mathcal{F}$ [47]. In a ternary system, as is the case here where a single fibre interacts with two immiscible fluid constituents, the free energy can be written as [48–50]

$$\mathcal{F} = \frac{k_\mathrm{B} T_0}{\mathrm{v}_0} \int_{\mathcal{V}} f(\phi_A, \phi_B, \phi)\, \mathrm{d}\mathbf{x}, \tag{27}$$

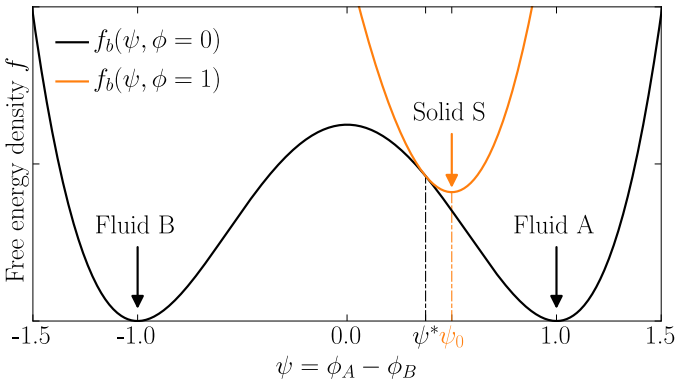

Figure 3: Bulk free energy density $f_b = f_0 + f_1$.

where $\mathcal{V}$ is the region of space occupied by the ternary system, k_B the Boltzmann constant, T_0 the reference temperature, v_0 a reference unit volume, f a non-dimensional free energy density yet to be defined, and $\mathrm{d}\mathbf{x}$ an infinitesimal volume element. The variables in the free energy density f are normally termed "order parameters"[51]. Because of the summation constraint $\phi_A + \phi_B + \phi = 1$, the free energy density can be conveniently recast as a function of two order parameters only, which are here $\psi = \phi_A - \phi_B$ and ϕ. For consistency purposes, the term ψ is hereafter referred to as the order parameter and ϕ as the fibre volume fraction. The following formulation, consistent with that of other authors also active in the field [42, 52], is suggested

$$f(\psi,\phi) = f_0(\psi) + f_1(\psi,\phi) + \frac{\xi^2}{2}|\nabla\psi|^2, \tag{28}$$

$$f_0(\psi) = \frac{1}{4}\left(1-\psi^2\right)^2, \tag{29}$$

$$f_1(\psi,\phi) = \frac{3}{2}\phi^2\left(\psi-\psi^*\right)^2, \tag{30}$$

where $f_0(\psi)$ is a double well function with a first minima located at $\psi = -1$ and a second minima located at $\psi = +1$, $f_1(\psi,\phi)$ is an additional term introduced to impose $\psi = \psi_0$ inside the fibre, ψ^* is a user-defined control parameter introduced to set the bead affinity, and ξ is the interfacial thickness defined in Equation 25. As seen in Figure 3, the bulk term $f_b = f_0 + f_1$ turns into a single well function with a minima located at $\psi = \psi_0$ inside each bead. The bulk term f_b essentially ensures that $\psi = +1$ in fluid constituent A, $\psi = -1$ in fluid constituent B, and $\psi = \psi_0$ in each solid bead. The last term $\xi^2|\nabla\psi|^2/2$ in Equation 28 is an interfacial term resulting in an energy excess across each diffuse interface. The control parameter ψ^* and the position of single well minimum ψ_0 are dependent on each other. Solving the functional derivative $\delta f_b/\delta\psi = 0$ gives the following dependency

$$\psi^* = \frac{2\psi_0 + \psi_0^3}{3}. \tag{31}$$

Imposing $\psi = \psi_0$ inside the solid constituent was originally suggested by Araki and Tanaka [53] to set the bead affinity.

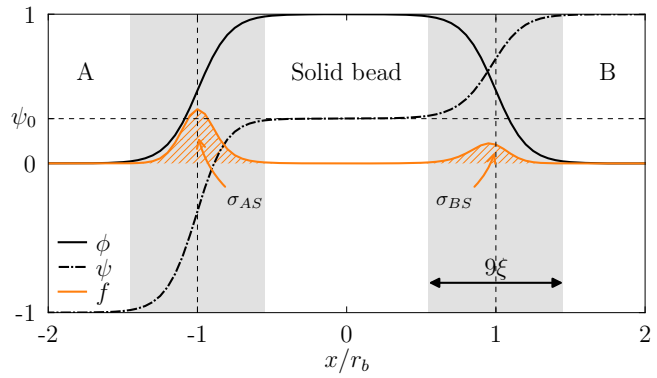

Figure 4: Free energy density $f(x)$ and order parameter $\psi(x)$ solved for the given smooth profile $\phi(x)$. The area in grey highlights the replacement of the sharp boundaries with two smoothly transitioning order parameters.

A positive value $\psi^* > 0$ results in a stronger affinity to fluid constituent A, while $\psi^* < 0$ results in a stronger bead affinity to constituent B. For $\psi^* = 0$ the bead has an equal affinity to the two fluid constituent. In fact, for the special case $\psi^* = 0$, it can be shown that the bulk term $\delta f_b/\delta\psi$ exactly coincides with that suggested by Kim [48] for a ternary fluid system, hence the coefficient 3/2 preceding the function f_1 in Equation 30. Note that, the term ψ^* is the actual input parameter, while the term ψ_0 is an output parameter. Yet, in all presented tests, the value ψ_0 delivered by the simulations exactly coincided with its theoretical counterpart worked out with Equation 31. Because it is straightforward to check that $\psi = \psi_0$ from an Eulerian contour, only the value of ψ_0 is specified hereafter. The order parameter $\psi(\boldsymbol{x}, t)$ is updated in time according to the following modified Cahn-Hilliard equation

$$\frac{\partial\psi}{\partial t} + \boldsymbol{u}\cdot\nabla\psi = M\nabla^2\mu_\psi \tag{32}$$

where M is the mobility of the binary fluid, $\boldsymbol{u}$ the Eulerian velocity field, and $\mu_\psi = \delta\mathcal{F}/\delta\psi$ the chemical potential with respect to the order parameter ψ. The formulation is somewhat different to that recently suggested by the same authors [30]. In fact, Equation 32 is easier to implement, is associated with a lower computational cost, and leads to more accurate simulation results. Figure 4 shows the one-dimensional equilibrium solutions of the total free energy density $f(x)$ and of the order parameter $\psi(x)$, both obtained for an arbitrarily set fibre volume fraction $\phi(x)$ and a zero velocity field $\boldsymbol{u} = \boldsymbol{0}$. The equilibrium solutions of Equation 32 were obtained with $\psi_0 = 0.3$ (value arbitrarily chosen), $\xi = 3\Delta$, and $\xi_c = 15\Delta$, where Δ is the unit grid spacing. It is seen that the model delivers expected solution profiles with respect to f and ψ. The free energy density f peaks at the sharp bead boundary defined by $\phi = 0.5$ and the order parameter ψ smoothly transitions over the same distance as that of the imposed smooth profile $\phi(x)$. The width of the transitional area is illustrated by the background area in grey.

2.5. Hydrodynamics

The total velocity field is here solved using the "Smooth Profile Method" [41]. In this method, the Eulerian velocity field is decomposed as $\boldsymbol{u} = (1-\phi)\boldsymbol{u} + \phi\boldsymbol{u}$, where the first term $(1-\phi)\boldsymbol{u}$ is the velocity field of the binary fluid and the second term $\phi\boldsymbol{u}$ is the velocity field of all beads. This latter, acting as a penalty term, is given by $\phi\boldsymbol{u} = \sum\phi_i[\boldsymbol{V}_i + \boldsymbol{\Omega}_i\times(\boldsymbol{x}-\boldsymbol{X}_i)]$. The smooth profile method is now well established and has been validated numerous times. Further reading and validations can be found in the works of Molina and Yamamoto [54] and those, more recent, of Molina et al. [26]. Elasto-capillary deformation occurs at submillimetric scales, where the capillary actions are the main drivers responsible for the fibre deformation. Unequal fluid densities and viscosities would only affect the unsteady dynamics and not the equilibrium state illustrated in Figure 1. For these reasons, a low-Reynolds-number flow with equal densities and viscosities in all constituents, that is $\rho_A = \rho_B = \rho$, and $\eta_A = \eta_B = \eta$, is considered. Hence, the two volume fractions ϕ_A and ϕ_B never appear in the implementation. The total velocity, which satisfies the incompressibility condition $\nabla\cdot\boldsymbol{u} = 0$, is advanced in time by solving the equation

$$\rho\frac{\partial\boldsymbol{u}}{\partial t} = -\nabla p + \eta\nabla^2\boldsymbol{u} + \rho\phi\boldsymbol{f}_\phi - \psi\nabla\mu_\psi - \phi\nabla\mu_\phi, \tag{33}$$

where $\boldsymbol{f}_\phi$ is the penalty term resulting from the fibre dynamics, and $\mu_\phi = \delta\mathcal{F}/\delta\phi$ is the chemical potential with respect to the fibre volume fraction ϕ. The last source term $-\phi\nabla\mu_\phi$ in Equation 33 did not appear in the original implementation [42], on which this work extends. The addition of this extra source term was motivated by the work of Boyer et al. [55], who suggested a Cahn-Hilliard formulation for ternary fluid systems. Our tests showed that this term was only necessary in two-dimensional simulations to improve stability. For three-dimensional simulations, the use of this term was not really needed and a remarkable match with the theory could be achieved [56].

2.6. Calculation of the capillary and hydrodynamic forces

A brief description of the overall numerical method is necessary to explain how the hydrodynamic and capillary forces are calculated. For a more complete description of the numerical method, the reader is referred to our previous work [30, 56, 57]. Let ψ^n be the order parameter calculated at the time t^n. The field ψ^{n+1} is first advanced in time using Equation 32. In the next stage, the mass centre $\boldsymbol{X}_i^{n+1}$ and the quaternion $\boldsymbol{q}_i^{n+1}$ of each bead are advanced in time using Equation 2 and Equation 3, respectively. A fractional step approach is then used to calculate the total velocity field. Using the momentum Equation 33, an intermediate velocity is first calculated as

$$\boldsymbol{u}^* = \boldsymbol{u}^n + \frac{1}{\rho}\int_{t^n}^{t^{n+1}}\left(-\nabla p^* + \eta\nabla^2\boldsymbol{u}^n - \psi^{n+1}\nabla\mu_\psi^{n+1} - \phi^{n+1}\nabla\mu_\phi^{n+1}\right)\mathrm{d}t \tag{34}$$

where p^* is an intermediate pressure calculated by solving the continuity equation $\nabla \cdot \boldsymbol{u}^* = 0$. The hydrodynamic and the capillary forces can then be calculated by assuming a momentum conservation between the i-th bead and the binary fluid. Since the hydrodynamic and the capillary contributions are accounted for in the calculation of the intermediate velocity, one obtains for the i-th spherical bead

$$\int_{t^n}^{t^{n+1}} \left(\boldsymbol{F}_i^h + \boldsymbol{F}_i^c\right) \mathrm{d}t = \rho \int_{\mathcal{V}} \phi_i^{n+1} \left(\boldsymbol{u}^* - \boldsymbol{u}_i^*\right) \mathrm{d}\mathbf{x} \tag{35}$$

$$\int_{t^n}^{t^{n+1}} \left(\boldsymbol{T}_i^h + \boldsymbol{T}_i^c\right) \mathrm{d}t = \rho \int_{\mathcal{V}} \phi_i^{n+1} \left(\boldsymbol{x} - \boldsymbol{X}_i\right) \times \left(\boldsymbol{u}^* - \boldsymbol{u}_i^*\right) \mathrm{d}\mathbf{x} \tag{36}$$

where $\boldsymbol{u}_i^* = \boldsymbol{V}_i^n + \boldsymbol{\Omega}_i^n \times (\boldsymbol{x} - \boldsymbol{X}_i^{n+1})$ is an intermediate velocity field associated with the i-th bead motion. The translational and rotational velocities of each bead are then advanced in time using Equation 5 and 6. Finally, the velocity field of the entire Lagrangian cloud is enforced onto the total fluid velocity field as

$$\boldsymbol{u}^{n+1} = \boldsymbol{u}^* + \int_{t^n}^{t^{n+1}} \left(-\frac{1}{\rho} \nabla p^{**} + \phi \boldsymbol{f}_\phi\right) \mathrm{d}t \tag{37}$$

where the pressure p^{**} is obtained from the incompressibility condition $\nabla \cdot \boldsymbol{u}^{n+1} = 0$. The time integral of the penalty term is calculated as

$$\int_{t^n}^{t^{n+1}} \phi \boldsymbol{f}_\phi \mathrm{d}t = \phi^{n+1} (\boldsymbol{u}_\phi^{n+1} - \boldsymbol{u}^*). \tag{38}$$

where $\phi^{n+1} \boldsymbol{u}_\phi^{n+1} = \sum \phi_i^{n+1} [\boldsymbol{V}_i^{n+1} + \boldsymbol{\Omega}_i^{n+1} \times (\boldsymbol{x} - \boldsymbol{X}_i^{n+1})]$. We also note that neither the Lagrangian forces $(\boldsymbol{F}^h + \boldsymbol{F}^c)$, nor the Lagrangian torques $(\boldsymbol{T}^h + \boldsymbol{T}^c)$, nor the penalty term $\phi \boldsymbol{f}_\phi$ need to be computed explicitly. Only their time integrals are required. The total pressure at time t^{n+1}, though not explicitly required in the following, is given by $p^{n+1} = p^* + p^{**}$

2.7. Intermediate conclusions to the suggested methods

The present work essentially combines three ingredients, namely a Lagrangian beam model, an Eulerian binary fluid model, and an Eulerian hydrodynamic model, which have been developed rather independently so far. The suggested formulation of the free energy also differs quite substantially from previous ones [42, 53], even though other approaches based on, for instance, the level-set method [43] would work equally well. Despite its associated high computational cost, a major strength of the model lies in its ability to simulate the unsteady three-dimensional elasto-capillary deformation of fibres at a fluidic interface. The model currently allows affordable simulations of a singe fibre made of up to twenty beads in a two-dimensional system and up to ten beads in three-dimensional system. Simulating the dynamics of much larger fibres is possible, yet it is associated with a much higher computational time. According to Yue et al. [58], using an adaptive mesh refinement across the interfaces could potentially reduce the computational time by up to 80 %. Finally, binary diffuse interface models are particularly attractive to simulate flows with moving contact lines [40]. Further research is however necessary for diffuse immersed walls, as is the case here with the fibre.

3. Results

The above equations were implemented in their non-dimensional form using the Reynolds number Re, the Weber number We, the Peclet number Pe, and the elasto-capillary number Ec defined as

$$Re = \frac{\rho_0 U_0 L_0}{\eta_0} \tag{39}$$

$$We = \frac{\rho_0 U_0^2 L_0}{\sigma_0} \tag{40}$$

$$Pe = \frac{U_0 L_0}{D_0} \tag{41}$$

$$Ec = \frac{k_0}{\sigma_0} \tag{42}$$

where $\rho_0 = \rho_A$ is the reference density, $\eta_0 = \eta_A$ the reference viscosity, $L_0 = \Delta$ the reference length, and U_0 a reference velocity arbitrarily set. It could for instance be the terminal velocity of a single bead in the reference fluid. The diffusion coefficient is defined as $D_0 = e_0 M$, where $e_0 = k_\mathrm{B} T_0 / \mathrm{v}_0$ is the reference free energy density seen in Equation 27. The reference surface tension is given by $\sigma_0 = e_0 L_0$. The term $k_0 = \pi r_b E / 2$, defined in Equation 11, is a reference measure of the fibre stiffness. The two limiting cases $Ec = 0$, respectively $Ec \to \infty$, indicate either loose beads in suspension or a fully rigid fibre. The overall dynamics of the ternary system were found to be quite sensitive to the ratio of the Weber number the Reynolds number We/Re. A Weber number greater or within the same order of magnitude as the Reynolds number resulted in a large oscillatory movement of the fibre at the fluidic A/B interface, which in turn resulted in unnecessarily long simulation times. An over-damped system led to a much better numerical stability. For these reasons, the Weber number is set to $We = 0.1$ and the Reynolds number to $Re = 0.01$ in all subsequent simulations.

3.1. Validation of the Lagrangian beam model

The overall performance of the beam model is dependent on the number of spherical beads N_b used to discretise the fibre. The following well-known test was therefore considered to work out the minimum number of beads necessary to obtain meaningful results. A fibre, initially set in horizontal position, had its left end fixed. That is, the

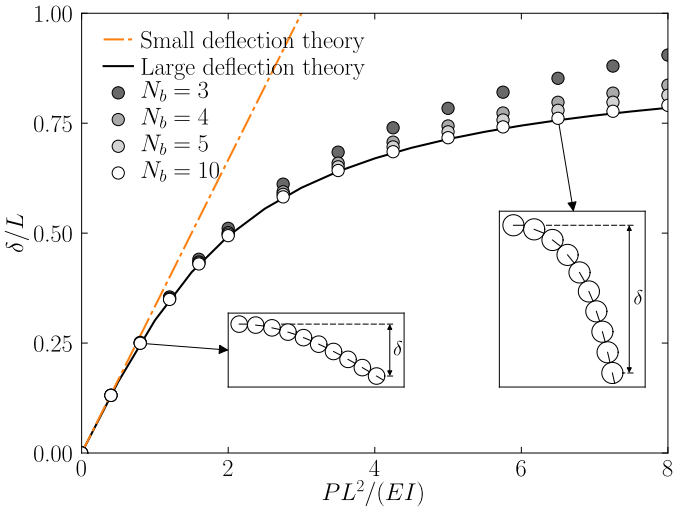

Figure 5: Bending of a fibre subject to a punctual load placed on its far right end. With $N_b = 10$, an excellent agreement is observed between the theoretical results and those obtained with the numerical beam model.

first bead had its position and velocities locked, $\boldsymbol{X}_{i=0} = \boldsymbol{0}$, $\boldsymbol{V}_{i=0} = \boldsymbol{0}$, and $\boldsymbol{\Omega}_{i=0} = \boldsymbol{0}$. The far right end of the fibre was subject to a downward point load P. An external force hence acted on the last bead as $\boldsymbol{F}^e_{i=N_b-1} = -P\boldsymbol{e}_y$. The deformation of the fibre was simulated for an increasing number of beads. The maximum vertical displacement δ, obtained at equilibrium, was calculated at the fibre extremity. Figure 5 shows the maximum vertical displacement δ as a function of the point load P. In the small-deflection theory, the maximum vertical displacement δ at the fibre extremity is given by

$$\frac{\delta}{L} = \frac{PL^2}{3EI}, \tag{43}$$

where $L = 2(N_b - 1)r_b$ is the length of the fibre and $I = \pi r_b^4/4$ is the area moment of inertia. The analytical solutions shown in Figure 5 for the large-deflection theory were provided by Fertis [12]. It is seen that, in the small deformation regime, that is $\delta/L < 1$, the beam model performs remarkably well irrespective of the number of beads in the fibre. For larger deformation, a number of beads equal or greater than $N_b \geq 10$ was necessary to achieve an accurate prediction of the bending.

3.2. Validation of the Eulerian hydrodynamic model

The calculation of hydrodynamic drag acting on a single sedimenting sphere has already been validated by the authors and showed an accuracy of about 10% in a low-Reynolds number flow, in both two- and three-dimensional systems [57]. Further three-dimensional validations of present Eulerian hydrodynamic model with respect to the hydrodynamic drag acting on non-spherical rigid bodies were also performed by Molina and Yamamoto [54]. Yet, an additional series of tests involving the two-dimensional motion of fibre immersed in a unary shear flow was here performed to validate the combination of the Eulerian hydrodynamic model with the Lagrangian beam model. The reference fluid constituent was sheared by an upper wall translating at a constant velocity U_w and by a lower wall translating in the opposite direction at the same velocity $-U_w$. Without any fibre in the domain, the solution of the velocity field is simply given by $\boldsymbol{u} = [(\gamma_0 y)\, 0]^\top$, where γ_0 is the resulting steady shear rate and y the vertical abscissa. At time $t = 0$, the fibre long axis was set perpendicular to the direction of the shear flow. Figure 6 illustrates the motion of a flexible fibre and that of a fairly rigid fibre. The results were obtained with $r_b = 6\Delta$, $\xi = \Delta$, $\xi_c = 3\Delta$, $Re = 0.01$, and $N = 180^2$, where N is the number of grid points used to discretise the two-dimensional domain. In a unary system, the transport Equation 28 does need not be solved. The values of the Weber and the Peclet numbers are hence irrelevant in this section. The results with respect to the flexible fibre were obtained with $k_0/(L_0\eta_0\gamma_0) = 15 \cdot 10^3$ and those with respect to the fairly rigid fibre with $k_0/(L_0\eta_0\gamma_0) = 75 \cdot 10^3$. The snaking motion of the flexible fibre along with the tumbling of the fairly rigid fibre closely resemble that previously observed by other authors [15, 19]. The orbit period of rotation T of the rigid fibre was also calculated as a function of the numbers of beads N_b forming the single fibre. Figure 7 compares the dimensionless period $\gamma_0 T$ with a polynomial function fitted to the data of Yamamoto and Matsuoka [15] and with the theoretical solution proposed by Jeffery [59], with the latter being further discussed in Appendix B. For $N_b \leq 9$, the quantitative predictions of the present model are in excellent agreement with the literature data. Because the length of the ten-bead fibre was almost as large as the height of the domain, a discrepancy is observed for $N_b = 10$. Further three-dimensional validations with respect to the tumbling motion of single rigid fibres in shears flow were performed by Kobayashi and Yamamoto [60, 61].

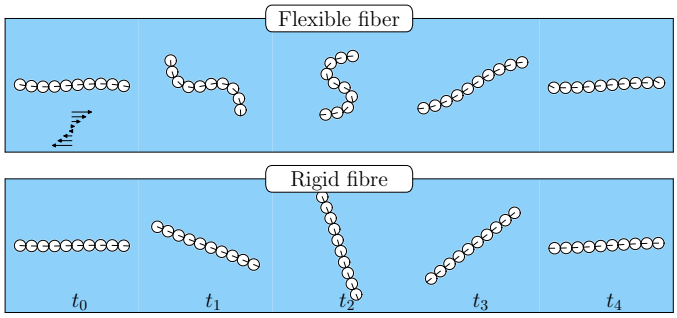

Figure 6: Dynamics of a flexible and a fairly rigid fibre in a unary shear flow ($N_b = 10$).

3.3. Validation of the Eulerian binary fluid model

To validate the Eulerian binary fluid model, the following test case was considered. A single bead was initially placed in a horizontally stratified binary system as illustrated in Figure 8. The upper half of the domain was filled with the fluid constituent A, that is $\psi = 1$, and the

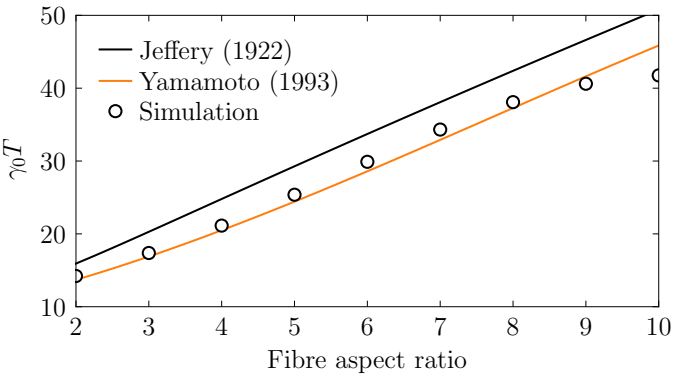

Figure 7: Orbit period ($\gamma_0 T$) of a rigid fibre as a function of the bead number N_b compared with literature data.

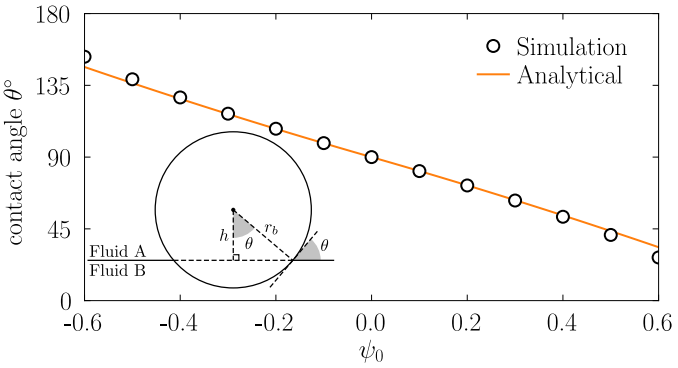

Figure 8: Contact angle as a function of the bead affinity parameter ψ_0.

lower half with the fluid constituent B, that is $\psi = -1$. At time $t = 0$, the bead centre of mass aligned with the horizontal A/B fluidic interface. A number of simulations were then performed for increasing values of the bead affinity parameter ψ_0. When the bead reached its equilibrium position, the geometric contact angle was calculated as $\theta = \cos^{-1}(h/r_b)$, where h was the shortest distance from the bead centre to the horizontal A/B fluidic interface. An analytical contact angle was also calculated using the energy excesses across each interfacial area. It was given by

$$\theta = \cos^{-1}\left(\frac{\sigma_{AS} - \sigma_{BS}}{\sigma_{AB}}\right), \tag{44}$$

where σ_{AS}, σ_{BS}, and σ_{AB} were the energy excesses respectively stored at the A/S interface, the B/S interface, and the A/B interface. The energy excesses σ_{AS} and σ_{BS} are illustrated in Figure 4. The theoretical value of the surface tension, that is the energy excess stored across the A/B interface, is given by $\sigma_{AB} = \sqrt{8}\sigma_0/3$. The comparison between the geometrically derived contact angle and its analytical counterpart is shown in Figure 8. The results were obtained with $r_b = 20\Delta$, $\xi = 3$, $\xi_c = 15\Delta$, $Re = 0.01$, $We = 0.1$, $Pe = 1$, and $N = 128^2$. For a contact angle within the range $40^\circ < \theta < 140^\circ$, the match turns out to be excellent. For contact angles outside this range, the error becomes larger. This is attributed to the difficulty

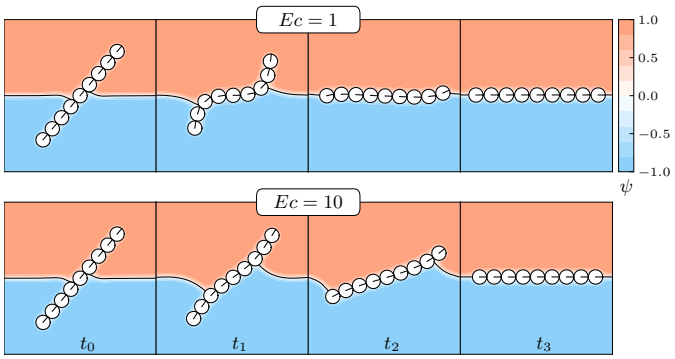

Figure 9: ψ-contour showing the capillary-induced tumbling of fibre, which has an equal affinity to the two fluid constituents, i.e. $\psi_0 = 0$.

in determining the geometric contact angle in the event of an almost complete bead dewetting.

3.4. Fibre in a horizontally stratified binary fluid

A set of simulations involving the capillary-induced tumbling of a fibre in a stratified fluid was here performed to qualitatively assess the full numerical model. Because the fluid is stagnant, no shear flow is imposed and so, the fibre rotation is solely driven by the capillary actions occurring at the three-phase contact line. These present results hence act as qualitative tests and allow us to verify the final orientation of the fibre attained at equilibrium. At time $t = 0$, the fibre was inclined by 50° with respect to the horizontal A/B fluidic interface. The upper half of the domain was also filled with the fluid constituent A, that is $\psi = 1$, and the lower half with the fluid constituent B, that is $\psi = -1$. The simulations were performed with the following input parameters $N_b = 9$, $r_b = 6\Delta$, $\xi = 2\Delta$, $\xi_c = 5\Delta$, $Re = 0.01$, $We = 0.1$, $Pe = 1$, and $N = 128^2$. In this section, the chosen input parameters result in a ratio of the interfacial length to bead radius equalled to $\xi/r_b = 1/3$. Simulations with smaller ratio down to 1/6 were also performed. Yet, we observed that the A/B fluidic interface rapidly "jumped" from one bead to the next one, making the unsteady dynamics rather unrealistic. The present ratio ξ_b/r_b led to a much smoother temporal evolution of A/B fluidic interface in the fibre vicinity. Figure 9 shows snapshots of the tumbling fibre exhibiting a neutral affinity to the two fluid constituents, that is $\psi_0 = 0$. The upper time sequence is shown for a highly deformable fibre, i.e. $Ec = 1$. The lower time sequence is shown for a more rigid fibre, i.e. $Ec = 10$. As expected, the long axis of the fibre eventually aligns with the A/B fluidic interface. Figure 10 shows the capillary-induced tumbling of a deformable fibre, which had a stronger affinity to the upper fluid A, that is $\psi_0 = 0.2$. The bottom portion of the fibre, initially immersed in the bottom fluid B, is pushed away towards the upper fluid A. This, in turn, causes an asymmetrical tumbling of the fibre. The above results show that the model is capable of simultaneously reproducing the capillary and deformability effects. The model was also

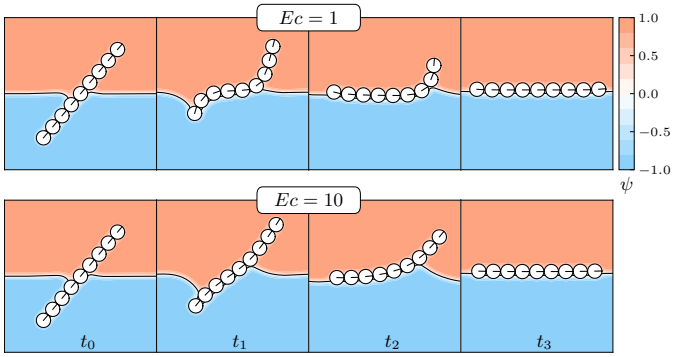

Figure 10: ψ-contour showing the capillary-induced tumbling of fibre, which has a stronger affinity to the upper fluid constituent A, i.e. $\psi_0 = 0.2$.

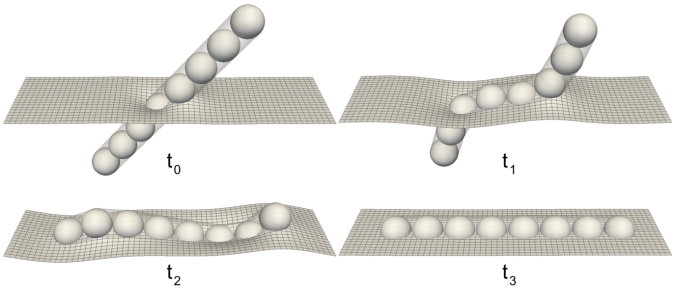

Figure 11: Capillary-induced tumbling of flexible fibre in a three-dimensional stratified system.

tested in three-dimensional systems. Figure 11 shows, for instance, the capillary-induced tumbling of a flexible fibre having identical affinity to the two fluid constituent in a three-dimensional stratified system. The checkered isosurface, defined as $\psi = 0$ represent the A/B fluidic interface. The three-dimensional results were obtained with $N_b = 8$, $r_b = 6$, $\xi = 2\Delta$, $\xi_c = 5\Delta$, $Re = 0.02$, $We = 0.1$, $Pe = 1$, $Ec = 10$, and $N = 120 \times 120 \times 32$. Further simulations can be found in the supplementary material.

3.5. Elasto-capillary bending of fibre by a fluid droplet

In this section, the bending of a fibre by a fluid droplet is investigated. At time $t = 0$, the droplet was initialised to a half-disk filled with the fluid constituent A, that is $\psi = 1$. The base of the half-disk was brought in contact with the horizontal fibre. The elasto-capillary number was here varied from $Ec = 10$ to $Ec = 1000$. The simulations were performed with three levels of bead affinity, namely with $\psi_0 = -0.2$, $\psi_0 = 0$, and $\psi_0 = 0.2$. With the exception of the domain size, which was here increased to $N = 256 \times 200$, the input parameters, set to $N_b = 18$, $r_b = 6\Delta$, $\xi = 2\Delta$, $\xi_c = 5\Delta$, $Re = 0.01$, $We = 0.1$, and $Pe = 1$ were identical to those used in the previous simulations of the capillary-induced fibre tumbling. Figure 12 shows the three equilibrium states obtained with a highly flexible fibre ($Ec = 10$), with an intermediately flexible fibre ($Ec = 40$), and with a rigid fibre ($Ec = 200$). The animated figure, available in the supplementary material,

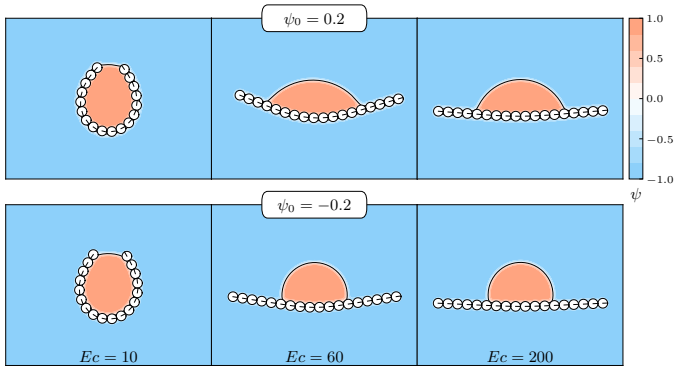

Figure 12: Encapsulation of the droplet by a highly flexible fibre. With greater elasto-capillary number only a partial wrapping is observed. Fully wrapping is observed for low fibre stiffness.

shows that model is capable of simulating the dynamics of the droplet encapsulation at low elasto-capillary number Ec. With increasing Ec, only partial wrapping occurs. Figure 12 shows the fibre curvature R_c as a function of Ec, where R_c was estimated by best-fitting a circle to the bended portion of the fibre (See Appendix Appendix C). The fibre curvature is here normalised with the equivalent droplet diameter $R_{droplet}$ defined in a two-dimensional domain by

$$\pi R_{droplet}^2 = \int_{\psi > 0.5} \psi \mathrm{d}\mathbf{x}. \tag{45}$$

The results demonstrate a linear dependency between the fibre curvature and the elasto-capillary number Ec, for both small and large structural deformation. This linear dependency has recently been confirmed experimentally by Schulman et al. [11] for single polymer fibres brought in contact to spherical glycerol droplets. The linear fit-coefficient α in the legend of Figure 13 indicates that a fibre with an affinity to the fluid droplet B ($\psi_0 < 0$) experiences a stronger bending than a fibre with an affinity to the reference surrounding fluid A ($\psi_0 > 0$). The increasing value of α with increasing ψ_0, as is the case here, is in fact expected. The linear trend also shows that upon encapsulation, which occurs at the left-end of the plot, the fibre curvature reaches a value very close to the droplet radius. This is also inline with the experimentally observed encapsulation, where the droplet radius was much larger than the bead radius. The model is also well capable of simulating the full and partial encapsulation of three-dimensional droplets. Figure 14 illustrates the three-dimensional equilibrium solutions, for which the fibre had an equal affinity to both fluid constituents, that is $\psi_0 = 0$. The droplet is represented by the isosurface $\psi = 0$. The unsteady dynamics of the ternary system during the process of encapsulation can be found in the supplementary material. Because the cost of three-dimensional simulations is expensive, not enough simulations data could be gained to verify the linear trend seen in two-dimensional simulations. The three-dimensional results were obtained with $N_b = 10$,

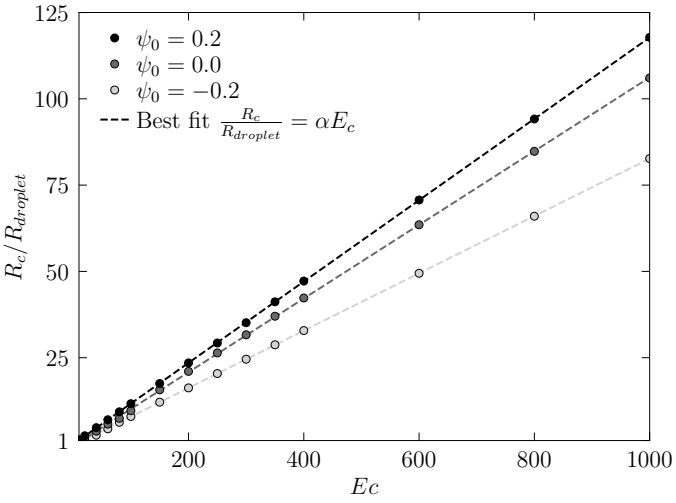

Figure 13: Linear dependency of the fibre curvature with the elasto-capillary number.

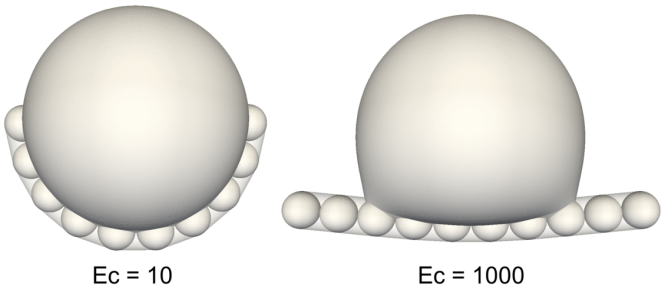

Figure 14: Three-dimensional equilibrium solutions of the droplet encapsulation for increasing Ec.

$r_b = 6$, $\xi = 2\Delta$, $\xi_c = 5\Delta$, $Re = 0.02$, $We = 0.1$, $Pe = 1$, and $N = 128 \times 120 \times 120$.

4. Conclusions

The investigation of flexible fibres in contact with liquid droplets has been receiving increasing attention in the recent years. Mostly steady-state, yet powerful, models derived using the variational approach, have been suggested in the literature. We here presented an alternative numerical approach to study the unsteady dynamics of a flexible fibre interacting with a fluidic interface. The present model combined a discrete element method to simulate the structural fibre deformation, a Cahn-Hilliard solver to track the fluidic interface, and a Navier-Stokes solver to simulate the low-Reynolds-number flow. Both the complete encapsulation and the partial wrapping of the fluid droplet by a flexible fibre could be simulated. In-line with previously reported experimental results, it was found that curvature of the fibre increases linearly with the square of the elasto-capillary length, for both low and large structural deformation. Future extension will allow the numerical investigation of more complex binary-fluid structure interactions [62], such as the elastocapillary self-folding of fibre [63], the capillary stretching of multiple fibres [64], and even the droplet encapsulation by a thin flexible sheet [4]. The present method could also be extended to investigate intricate industrial applications, where the hydrodynamics and the elasto-capillary effects play equally important roles. Such an application could for instance involve the rise of air bubbles across a cloud of flexible fibres suspended in water.

Acknowledgement

The last author, T. Taniguchi, gratefully acknowledges the financial support of the Hosokawa Powder Technology Foundation (Heisei-30, Kenkyu Jyosei). This work was also partially supported by a Marie Curie International Outgoing Fellowship with the European Union Seventh Framework Program for Research and Technological Development (2007-2013) under the grant agreement number 623518.

Appendix A.

The following procedure describes the frame transformation $\boldsymbol{X}_i \boldsymbol{e}_x \boldsymbol{e}_y \boldsymbol{e}_z \rightarrow \boldsymbol{X}_i \boldsymbol{e}_{x'} \boldsymbol{e}_{y'} \boldsymbol{e}_{z'}$. The unit quaternion $\boldsymbol{q}^*$, associated with the unit vector transformation $\boldsymbol{e}_{x'} = \boldsymbol{R}^* \cdot \boldsymbol{e}_x$, where $\boldsymbol{R}^*$ is a rotation matrix yet to be defined, is first calculated as

$$\boldsymbol{q}^* = \begin{bmatrix} q_s^* \\ q_x^* \\ q_y^* \\ q_z^* \end{bmatrix} = \frac{[q_s\, q_x\, q_y\, q_z]^\top}{\left(q_s^2 + q_x^2 + q_y^2 + q_z^2\right)^{1/2}}, \tag{A.1}$$

where $q_s = 1 + (\boldsymbol{e}_x \cdot \boldsymbol{e}_{x'})$ is calculated using the vectorial dot product and $[q_x\, q_y\, q_z]^\top = \boldsymbol{e}_x \times \boldsymbol{e}_{x'}$ is the vectorial cross product. Leaving out the asterisk superscript for better readability, the transformation matrix of any quaternion $[q_s\, q_x\, q_y\, q_z]$ is given by [27]

$$\mathbf{R} = 2 \begin{bmatrix} \frac{1}{2} - q_y^2 - q_z^2 & q_y q_x - q_s q_z & q_z q_x + q_s q_y \\ q_x q_y + q_s q_z & \frac{1}{2} - q_x^2 - q_z^2 & q_z q_y - q_s q_x \\ q_x q_z - q_s q_y & q_y q_z + q_s q_x & \frac{1}{2} - q_x^2 - q_y^2 \end{bmatrix}. \tag{A.2}$$

The remaining two unit vectors forming the local beam frame are now computed by transforming the unit vectors of the inertial frame as $\boldsymbol{e}_{y'} = \boldsymbol{R}^* \cdot \boldsymbol{e}_y$ and $\boldsymbol{e}_{z'} = \boldsymbol{R}^* \cdot \boldsymbol{e}_z$.

Appendix B.

A prolate particle with aspect ratio e_p exhibits a periodic motion when placed in a laminar shear flow. The prolate actually spends most of its time aligned with the shear direction, but every half a period it rapidly tumbles by 180° [65]. The rotation period of the prolate is given by [59]

$$T = \frac{2\pi}{\gamma_0} \left(e_p + \frac{1}{e_p} \right). \tag{B.1}$$

The equivalent aspect ratio of a cylindrical fibre e_c is conveniently estimated as $e_c = 1.14 e_p^{0.844}$ [66].

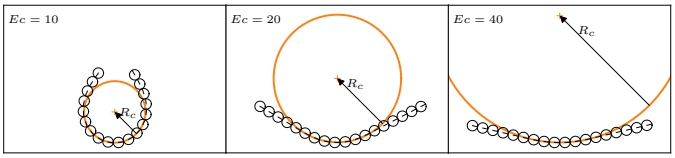

Figure C.15: Estimation of the fibre curvature R_c using the method of least squares.

Appendix C.

The fibre curvature is estimated by taking the radius R_c of a circle fitted with the method of least squares to six successive bead centres. Figure C.15 shows a series of circles fitted to deformed fibres obtained for the following elasto-capillary numbers $Ec = 10$, $Ec = 20$, and $Ec = 40$.

[1] J. M. Preston, S. Saha, Froth flotation of fibres, Journal of the Textile Institute Transactions 40 (1949) 381–388.

[2] J. Redlinger-Pohn, M. Grabner, P. Zauner, S. Radl, Separation of cellulose fibres from pulp suspension by froth flotation fractionation, Separation and Purification Technology 169 (2016) 304–313.

[3] X. Guo, H. Li, B. Yeop Ahn, E. Duoss, K. Hsia, J. Lewis, R. Nuzzo, Two- and three-dimensional folding of thin film single-crystalline silicon for photovoltaic power applications, Proceedings of the National Academy of Sciences 106 (2009) 20149–20154.

[4] C. Py, P. Reverdy, L. Doppler, J. Bico, B. Roman, C. Baroud, Capillary origami: spontaneous wrapping of a droplet with an elastic sheet, Physical Review Letters 98 (2007) 156103.

[5] S. Lam, K. Velikov, O. Velev, Pickering stabilization of foams and emulsions with particles of biological origin, Current Opinion in Colloid & Interface Science 19 (2014) 490–500.

[6] R. Style, L. Isa, E. Dufresne, Adsorption of soft particles at fluid interfaces, Soft Matter 11 (2015) 7412–7419.

[7] C. Duprat, S. Protiere, A. Beebe, H. Stone, Wetting of flexible fibre arrays, Nature 11 (2012) 510–513.

[8] B. Roman, J. Bico, Elasto-capillarity: deforming an elastic structure with a liquid droplet, Journal of Physics: Condensed Matter 22 (2010) 493101.

[9] S. Neukirch, A. Antkowiak, J. Marigo, The bending of an elastic beam by a liquid drop: a variational approach, Proceedings of the Royal Society A: Mathematical, Physical and Engineering Sciences 469 (2013) 20130066.

[10] N. Brubaker, J. Lega, Two-dimensional capillary origami, Physics Letters A 380 (2016) 83–87.

[11] R. Schulman, A. Porat, K. Charlesworth, A. S. T. Fortais, E. Raphael, K. Dalnoki-Veress, Elastocapillary bending of microfibers around liquid droplets, Soft Matter 13 (2017) 720–724.

[12] D. Fertis, Nonlinear mechanics, Taylor & Francis, 1993.

[13] O. Gupta, Finite and boundary element methods in engineering, Taylor & Francis, 1999.

[14] O. du Roure, A. Lindner, E. Nazockdast, M. Shelley, Dynamics of flexible fibers in viscous flows and fluids, Annual Review of Fluid Mechanics 51 (2019) 539–572.

[15] S. Yamamoto, T. Matsuoka, A method for dynamic simulation of rigid and flexible fibers in a flow field, The Journal of Chemical Physics 98 (1993) 644–650.

[16] R. Ross, D. Klingenberg, Dynamic simulation of flexible fibers composed of linked rigid bodies, The Journal of Chemical Physics 106 (1997) 2949–2960.

[17] P. Skjetne, R. Ross, D. Klingenberg, Simulation of single fiber dynamics, The Journal of Chemical Physics 107 (1997) 2108–2121.

[18] Z. Ning, J. Melrose, A numerical model for simulating mechanical behavior of flexible fibers, The Journal of Chemical Physics 111 (1999) 10717–10726.

[19] K. Kabanemi, J. Hetu, Effects of bending and torsion rigidity on deformation and breakage of flexible fibers: A direct simulation study, The Journal of Chemical Physics 136 (2012) 074903.

[20] Z. Pei, Y. Zhang, J. Zhou, A model for the particle-level simulation of multiple flexible fibers moving in a wall-bounded fluid flow, Journal of Fluids and Structures 80 (2018) 37–58.

[21] Y. Liu, B. Chakrabarti, D. Saintillan, A. Lindner, O. du Roure, Morphological transitions of elastic filaments in shear flow, Proceedings of the National Academy of Sciences of the United States of America 115 (2018) 9438–9443.

[22] M. Dotto, M. Marchioli, Orientation, distribution, and deformation of inertial flexible fibers in turbulent channel flow, Acta Mechanica 230 (2019) 597–621.

[23] C. Coetzee, Review: calibration of the discrete element method, Powder Technology 310 (2017) 104–142.

[24] Y. Guo, C. Wassgren, B. Hancock, W. Ketterhagen, J. Curtis, Validation and time step determination of discrete element modeling of flexible fibers, Powder Technology 249 (2013) 386–395.

[25] J. Kim, Phase-field models for multi-component fluid flows, Communications in Computational Physics 12 (2012) 613–661.

[26] J. Molina, K. Otomura, H. Shiba, H. Kobayashi, M. Sano, R. Yamamoto, Rheological evaluation of colloidal dispersions using the smoothed profile method: formulation and applications, Journal of Fluid Mechanics 792 (2016) 590–619.

[27] L. Huang, A concise introduction to mechanics of rigid bodies: multidisciplinary engineering. Second edition, Springer, 2016.

[28] F. Zhao, B. van Wachem, A novel Quaternion integration approach for describing the behaviour of non-spherical particles, Acta Mechanica 224 (2013) 3091–3109.

[29] G. Lecrivain, R. Rayan, A. Hurtado, U. Hampel, Using quasi-DNS to investigate the deposition of elongated aerosol particles in a wavy channel flow, Computers & Fluids 124 (2016) 78–85.

[30] G. Lecrivain, R. Yamamoto, U. Hampel, T. Taniguchi, Direct numerical simulation of an arbitrarily shaped particle at a fluidic interface, Physical Review E 95 (2017) 063107.

[31] P. Cundall, O. Strack, A discrete numerical model for granular assemblies, Geotechnique 29 (1) (1979) 47–65.

[32] D. Potyondy, P. Cundall, A bonded-particle model for rock, International Journal of Rock Mechanics and Mining Sciences 41 (8) (2004) 1329–1364.

[33] F. Wittel, H. Carmona, F. Kun, Mechanisms in impact fragmentation, International Journal of Fracture 154 (2008) 105–117.

[34] H. Carmona, F. Wittel, F. Kun, H. Herrmann, Fragmentation processes in impact of spheres, Physical Review E 77 (2008) 051302.

[35] M. Obermayr, K. Dressler, C. Vrettos, P. Eberhard, A bonded-particle model for cemented sand, Computers and Geotechnics 49 (2013) 299–313.

[36] D. Nguyen, N. Kang, J. Park, Validation of partially flexible rod model based on discrete element method using beam deflection and vibration, Powder Technology 237 (2013) 147–152.

[37] N. Nan, Y. Wang, H. Tang, A viscoelastic model for flexible fibers with material damping, Powder Technology 276 (2015) 175–182.

[38] Y. Guo, J. Curtis, Discrete element method simulations for complex granular flows, Annual Review of Fluid Mechanics 47 (2015) 21–46.

[39] A. Andre, I. Iordanoff, J. Charles, J. Neauport, Discrete element method to simulate continuous material by using the cohesive beam model, Computer Methods in Applied Mechanics and Engineering 213-216 (2012) 113–125.

[40] R. Borcia, I. Borcia, M. Helbig, M. Meier, C. Egbers, M. Bestehorn, Dancing drops over vibrating substrates, The European Physical Journal Special Topics 226 (2017) 1297–1306.

[41] Y. Nakayama, R. Yamamoto, Simulation method to resolve hydrodynamic interactions in colloidal dispersions, Physical Review E 71 (2005) 036707.

[42] H. Shinto, Computer simulation of wetting, capillary forces,

and particle-stabilized emulsions: From molecular-scale to mesoscale modeling, Advanced Powder Technology 23 (2012) 538–547.
[43] M. Fujita, O. Koike, Y. Yamaguchi, Direct simulation of drying colloidal suspension on substrate using immersed free surface model, Journal of Computational Physics 281 (2015) 421–448.
[44] H. Hwang, G. Son, A level-set method for the direct numerical simulation of particle motion in droplet evaporation, Numerical Heat Transfer, Part B: Fundamentals 68 (2015) 479–494.
[45] X. Sun, M. Sakai, Direct numerical simulation of gas-solid-liquid flows with capillary effects: an application to liquid bridge forces between spherical particles, Physical Review E 94 (2016) 063301.
[46] P. Yue, J. Feng, C. Liu, J. Shen, A diffuse-interface method for simulating two-phase flows of complex fluids, Journal of Fluid Mechanics 515 (2004) 293–317.
[47] M. Cates, E. Tjhung, Theories of binary fluid mixtures: from phase-separation kinetics to active emulsions, Journal of Fluid Mechanics 836 (2018) P1.
[48] J. Kim, Phase field computations for ternary fluid flows, Computer Methods in Applied Mechanics and Engineering 196 (2007) 4779–4788.
[49] P. Millett, Y. Wang, Diffuse-interface field approach to modeling arbitrarily-shaped particles at fluid-fluid interfaces, Journal of Colloid and Interface Science 353 (1) (2011) 46–51.
[50] S. Minjeaud, An unconditionally stable uncoupled scheme for a triphasic Cahn-Hilliard/Navier-Stokes model, Numerical Methods for Partial Differential Equations 29 (2013) 584–618.
[51] D. Anderson, G. McFadden, A. Wheeler, Diffuse interface methods in fluid mechanics, Annual Review of Fluid Mechanics 30 (1998) 139–165.
[52] T. Araki, S. Fukai, Controlled motion of Janus particles in periodically phase-separating binary fluids, Soft Matter 11 (2015) 3470–3479.
[53] T. Araki, H. Tanaka, Wetting-induced depletion interaction between particles in a phase-separating liquid mixture, Physical Review E 73 (2006) 061506.
[54] J. Molina, R. Yamamoto, Direct numerical simulations of rigid body dispersions. I. Mobility/friction tensors of assemblies of spheres, The Journal of Chemical Physics 139 (2013) 234105.
[55] F. Boyer, C. Lapuerta, S. Minjeaud, B. Piar, M. Quintard, Cahn-Hilliard/Navier-Stokes model for the simulation of three-phase flows, Transport in Porous Media 82 (2010) 463–483.
[56] G. Lecrivain, Y. Kotani, R. Yamamoto, U. Hampel, T. Taniguchi, Diffuse interface model to simulate the rise of a fluid droplet across a cloud of particles, Physical Review Fluids 3 (2018) 094002.
[57] G. Lecrivain, R. Yamamoto, U. Hampel, T. Taniguchi, Direct numerical simulation of a particle attachment to an immersed bubble, Physics of Fluids 28 (2016) 083301.
[58] P. Yue, C. Zhou, J. Feng, C. Ollivier-Gooch, H. Hu, Phase-field simulations of interfacial dynamics in viscoelastic fluids using finite elements with adaptive meshing, Journal of Computational Physics 219 (2006) 47 – 67.
[59] G. Jeffery, The motion of ellipsoidal particles immersed in a viscous fluid, Proceedings of the Royal Society of London A 102.
[60] H. Kobayashi, R. Yamamoto, Tumbling motion of a single chain in shear flow: A crossover from Brownian to non-Brownian behavior, Physical Review E 81 (2010) 041807.
[61] H. Kobayashi, R. Yamamoto, Reentrant transition in the shear viscosity of dilute rigid-rod dispersions, Physical Review E 84 (2011) 051404.
[62] M. Roudbari, E. van Brummelen, Binary-fluid–solid interaction based on the Navier-Stokes-Korteweg equations, Mathematical Models and Methods in Applied Sciences 29 (2019) 995–1036.
[63] A. Evans, S. Spagnolie, D. Bartolo, E. Lauga, Elastocapillary self-folding: buckling, wrinkling, and collapse of floating filaments, Soft Matter 9 (2013) 1711–1720.
[64] C. Duprat, S. Protiere, Capillary stretching of fibers, Europhysics Letters 111 (2015) 56006.
[65] K. Moses, S. Advani, A. Reinhardt, Investigation of fiber motion near solid boundaries in simple shear flow, Rheologica Acta 40 (2001) 296–306.
[66] J. Harris, J. Pittman, Equivalent ellipsoidal axis ratios of slender rod-like particles, Journal of Colloid and Interface Science 50 (1975) 280 – 282.